Inorganic Chemistry

Article

pubs.acs.org/IC

Crystal Growth and Characterization of the Narrow-Band-Gap Semiconductors $OsPn_2$ (Pn = P, As, Sb)

Daniel E. Bugaris,[†] Christos D. Malliakas,[†,‡] Daniel P. Shoemaker,[†] Dat T. Do,[§] Duck Young Chung,[†] Subhendra D. Mahanti,[§] and Mercouri G. Kanatzidis*[,†,‡]

[†]Materials Science Division, Argonne National Laboratory, Argonne, Illinois 60439, United States

[‡]Department of Chemistry, Northwestern University, Evanston, Illinois 60208, United States

[§]Department of Physics and Astronomy, Michigan State University, East Lansing, Michigan 48824, United States

Supporting Information

ABSTRACT: Using metal fluxes, crystals of the binary osmium dipnictides $OsPn_2$ (Pn = P, As, Sb) have been grown for the first time. Single-crystal X-ray diffraction confirms that these compounds crystallize in the marcasite structure type with orthorhombic space group *Pnnm*. The structure is a three-dimensional framework of corner- and edge-sharing $OsPn_6$ octahedra, as well as $[Pn_2^{4-}]$ anions. Raman spectroscopy shows the presence of P−P single bonds, consistent with the presence of $[Pn_2^{-4}]$ anions and formally Os^{4+} cations. Optical-band-gap and high-temperature electrical resistivity measurements indicate that these materials are narrow-band-gap semiconductors. The experimentally determined Seebeck coefficients reveal that nominally undoped OsP_2 and $OsSb_2$ are n-type semiconductors, whereas $OsAs_2$ is p-type. Electronic band structure using density functional theory calculations shows that these compounds are indirect narrow-band-gap semiconductors. The bonding p orbitals associated with the Pn_2 dimer are below the Fermi energy, and the corresponding antibonding states are above, consistent with a Pn−Pn single bond. Thermopower calculations using Boltzmann transport theory and constant relaxation time approximation show that these materials are potentially good thermoelectrics, in agreement with experiment.

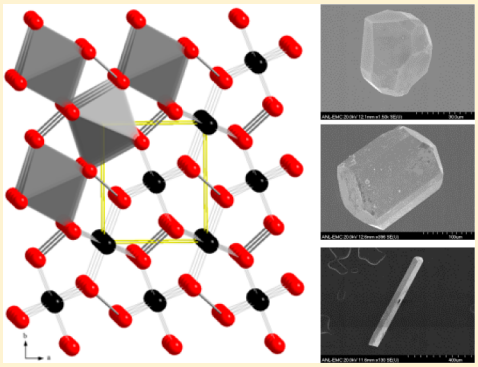

INTRODUCTION

Interest in transition-metal pnictides has revived with the discovery of high-temperature superconductivity in iron arsenides.[1] Although superconductivity has mostly been limited to ternary and quaternary transition-metal pnictides, the binary phases have been studied extensively as well, albeit for different reasons. One particular class of binary transition-metal pnictides that has drawn significant attention is the transition-metal dipnictides, MPn_2 (M = transition metal; Pn = P, As, Sb), many of which crystallize in the marcasite-type structure.

Named for the mineral marcasite (FeS_2), this structure type[2] encompasses a wide array of transition-metal pnictides and chalcogenides. The marcasite-type compound $FeSb_2$ has been shown to be a rare example of a highly correlated diamagnetic narrow-band-gap semiconductor and/or a Kondo insulator (similar to FeSi).[3] Because of its colossal thermoelectric power factor (~2300 $\mu W\ K^{-2}\ cm^{-1}$ at 12 K and ~8000 $\mu W\ K^{-2}\ cm^{-1}$ at 28 K),[4] $FeSb_2$ has been investigated as a cryogenic thermoelectric material. However, its thermoelectric figure of merit (ZT) remains limited by the relatively high thermal conductivity. Various strategies have been pursued to improve the magnetotransport properties of $FeSb_2$, including doping with cobalt,[5] chromium,[6] arsenic,[7] tin,[8] and tellurium,[9] as well as spark-plasma sintering of nanoparticles,[10] but none have yet resulted in a significant improvement in ZT.

In contrast to the considerable effort spent on studying $FeSb_2$ and to a lesser extent its lighter group V analogues, FeP_2 (a possible electrode for lithium batteries)[11] and $FeAs_2$ (a thermoelectric material),[12] there has been minimal investigation of the isostructural ruthenium and osmium pnictide marcasites. Although the syntheses of RuP_2, OsP_2, and $RuAs_2$ were first reported in the 1930s,[13] the unit cell lattice parameters and marcasite crystal structure for these compounds and the arsenide/antimonide variants were not determined by powder X-ray diffraction until the 1960s[14] and were confirmed by powder neutron diffraction in the 1970s.[15] Measurements revealed all six compounds to be diamagnetic, small-band-gap semiconductors below room temperature.[16]

Herein we report a more detailed investigation of the marcasite-type $OsPn_2$ (Pn = P, As, Sb) binary compounds. To the best of our knowledge, this is the first instance where these materials have been grown as single crystals, which has been accomplished via the use of metal fluxes. The marcasite-type crystal structure previously determined by powder X-ray and neutron diffraction has been confirmed via single-crystal X-ray diffraction. The presence of a P−P single bond in OsP_2 is observed with Raman spectroscopy. This is consistent with the

Received: July 18, 2014
Published: August 27, 2014

   dx.doi.org/10.1021/ic501733z | Inorg. Chem. 2014, 53, 9959−9968

Table 1. Structure Refinement Details from Single-Crystal X-ray Diffraction for $OsPn_2$ (Pn = P, As, Sb)[a]

	OsP_2	$OsAs_2$	$OsSb_2$
fw	252.14	340.04	433.70
temperature (K)	120(2)	298(2)	298(2)
a (Å)	5.084(1)	5.406(1)	5.938(1)
b (Å)	5.874(1)	6.175(1)	6.696(1)
c (Å)	2.9041(6)	2.9941(6)	3.2044(6)
volume (Å^3)	86.73(3)	99.94(3)	127.41(4)
ρ_c (g cm^{-3})	9.655	11.300	11.305
μ (mm^{-1})	74.763	96.137	70.385
F(000)	212	284	356
cryst size (mm^3)	0.074 × 0.056 × 0.043	0.214 × 0.084 × 0.082	0.268 × 0.049 × 0.036
θ range for data collection (deg)	5.30−34.90	5.01−35.00	4.59−29.10
index ranges	$-8 \le h \le 7$, $-9 \le k \le 9$, $-4 \le l \le 4$	$-7 \le h \le 8$, $-9 \le k \le 9$, $-4 \le l \le 4$	$-8 \le h \le 8$, $-9 \le k \le 8$, $-4 \le l \le 4$
reflns collected	1232	1380	1069
indep reflns	225 [R_{int} = 0.0412]	251 [R_{int} = 0.0877]	193 [R_{int} = 0.0814]
completeness to θ = 34.90° (%)	100	100	97
data/restraints/param	225/0/12	251/0/12	193/0/12
GOF	1.528	1.272	1.190
final R indices [$I > 2\sigma(I)$][b]	R_{obs} = 0.0187, wR_{obs} = 0.0424	R_{obs} = 0.0285, wR_{obs} = 0.0671	R_{obs} = 0.0371, wR_{obs} = 0.0895
R indices [all data][b]	R_{all} = 0.0193, wR_{all} = 0.0427	R_{all} = 0.0288, wR_{all} = 0.0673	R_{all} = 0.0371, wR_{all} = 0.0895

[a]For all structures, λ = 0.71073 Å, the space group is *Pnnm*, and Z = 2. [b]$R = \sum||F_o| - |F_c||/\sum|F_o|$, $wR = \{\sum[w(|F_o|^2 - |F_c|^2)^2]/\sum[w(|F_o|^4)]\}^{1/2}$ and calcd $w = 1/[\sigma^2(F_o^2) + (AP)^2 + (BP)]$ where $P = (F_o^2 + 2F_c^2)/3$. For OsP_2, A = 0.0124 and B = 0.2663. For $OsAs_2$, A = 0.0204 and B = 1.7820. For $OsSb_2$, A = 0.0672 and B = 0.1111.

formal oxidation assignments of Os^{4+} and $[P_2^{4-}]$ (or generally $[Pn_2^{4-}]$). From IR and UV−vis−near-IR (NIR) spectroscopy, the optical band gaps are determined to be 0.21(1), 0.92(1), and 1.13(2) eV for $OsSb_2$, $OsAs_2$, and OsP_2, respectively. High-temperature electrical resistivity and Seebeck measurements in nominally undoped compounds characterize all three as narrow-band-gap semiconductors, with electrons being the dominant charge carriers in OsP_2 and $OsSb_2$, whereas holes are the dominant charge carrier in $OsAs_2$. Electronic band structure calculations support the results from the band-gap, Raman, and charge-transport measurements.

EXPERIMENTAL METHODS

General Details. The following reagents were used as received: osmium powder (J&J Materials Inc., 99.98%), red phosphorus (Aldrich, >99.99%), tin shot (Cerac, 99.9%), and iodine (Aldrich). Arsenic lumps (Alfa Aesar, 99.99999+%) and antimony pieces (Cerac, 99.999%) were ground to a coarse powder prior to use. Initial manipulations were carried out in an M-Braun glovebox under an inert argon atmosphere (<0.1 ppm of H_2O and O_2).

Synthesis of OsP_2. The reaction mixture consisted of osmium (0.190 g, 1 mmol), phosphorus (0.077 g, 2.5 mmol), and tin (6 g, 50 mmol). The reagents were loaded into a thin niobium tube that had been sealed at both ends with a Centor arc welder. Next, the niobium tube was placed in a 15 mm o.d. × 13 mm i.d. fused-silica tube, which was flame-sealed under a vacuum of $<10^{-4}$ mbar. In a programmable furnace, the tube was heated to 1050 °C in 12 h, held at 1050 °C for 24 h, and then slowly cooled to room temperature over 72 h. The fused-silica tube was opened, and the niobium tube was removed. One end of the niobium tube was cut off before it was loaded into a new fused-silica tube. A stainless steel frit was placed on top of the niobium tube, and the fused-silica tube was sealed under a vacuum of $<10^{-4}$ mbar. The fused-silica tube was placed in a furnace that had been preheated to 520 °C and was allowed to soak for 15 min in order to fully melt the tin flux. The fused-silica tube was then removed from the furnace and centrifuged. Small black prismatic crystals of OsP_2, as well as black polycrystalline OsP_2, were mechanically removed from the interior of the niobium tube. Residual tin flux could be removed by soaking the product in dilute HCl (1:3 H_2O), followed by isolation of OsP_2 by gravity filtration and rinsing with H_2O and acetone. The yield was 100% based on osmium according to powder X-ray diffraction.

Pure polycrystalline OsP_2 could be prepared by two different methods. In the first, a 1:3 mixture of osmium and phosphorus with a total mass of approximately 0.36 g was loaded directly into a 9 mm o.d. × 7 mm i.d. fused-silica tube with 3 g of tin. After the tube was sealed under vacuum, it was heated in a furnace to 1050 °C in 12 h and held at 1050 °C for 48 h, and then the furnace was turned off. After the fused-silica tube was opened at room temperature, the solidified tin ingot was placed directly in dilute HCl (1:3 H_2O). Once the tin was dissolved, OsP_2 could be recovered by gravity filtration. For the second method, a 1:3 mixture of osmium and phosphorus with a total mass of approximately 0.25 g was loaded directly into a 12 mm o.d. × 10 mm i.d. fused-silica tube with 0.2 g of I_2, which acts as a mineralizer. After the tube was sealed under vacuum, it was then heated in a furnace to 1000 °C in 12 h, held at 1000 °C for 192 h, and then cooled to room temperature in 12 h. After the fused-silica tube was opened, pure polycrystalline OsP_2 was found at one end, and crystallized I_2 (or PI_3) was found at the opposite end.

Synthesis of $OsAs_2$. The reaction mixture consisted of osmium (0.190 g, 1 mmol), arsenic (0.187 g, 2.5 mmol), and tin (6 g, 50 mmol). The procedure is analogous to that of OsP_2, except that the reaction was cooled to room temperature over 96 h instead of 72 h. Following centrifugation, small black prismatic crystals of $OsAs_2$, in addition to black polycrystalline material, were found inside the niobium tube. Residual tin flux could be removed by soaking the product in dilute HCl (1:3 H_2O), followed by isolation of the product by gravity filtration and rinsing with H_2O and acetone. According to powder X-ray diffraction, the product contained approximately 95% $OsAs_2$ and 5% unreacted osmium.

In order to obtain a pure polycrystalline sample of $OsAs_2$, the original product from the tin flux reaction that contains unreacted osmium can be reacted with excess arsenic. The mixture containing 95% $OsAs_2$ and 5% osmium was ground together with arsenic (10% by weight) using a mortar and pestle and loaded into a 9 mm o.d. × 7 mm i.d. fused-silica tube. After the tube was sealed under vacuum, it was heated in a furnace to 1050 °C in 6 h and held at 1050 °C for 48 h, and then the furnace was turned off. A solidified mass of phase-pure $OsAs_2$ (according to powder X-ray diffraction) was found at the

dx.doi.org/10.1021/ic501733z | Inorg. Chem. 2014, 53, 9959−9968

bottom of the tube, and the excess arsenic collected on the other end of the tube. Conversely, pure polycrystalline $OsAs_2$ can also be prepared by the I_2 mineralizer route described above for OsP_2.

Synthesis of $OsSb_2$. The reaction mixture consisted of osmium (0.150 g, 0.789 mmol) and antimony (3.553 g, 29 mmol). The reagents were loaded into a 12 mm o.d. × 10 mm i.d. fused-silica tube, which was flame-sealed under a vacuum of $<10^{-4}$ mbar. This fused-silica tube was then flame-sealed under vacuum in a secondary 15 mm o.d. × 13 mm i.d. fused-silica tube. In a programmable furnace, the tube was heated at 100 °C h^{-1} to 1150 °C, held at 1150 °C for 48 h, and cooled at 5 °C h^{-1} to 600 °C, and finally the furnace was turned off to allow the reaction to rapidly cool to room temperature. The outer fused-silica tube was opened, and the smaller fused-silica tube was removed. One end of the smaller fused-silica tube was scored and carefully opened. This smaller fused-silica tube was loaded into a new 15 mm o.d. × 13 mm i.d. fused-silica tube, a steel frit was placed on top, and the outer tube was sealed under a vacuum of $<10^{-4}$ mbar. The fused-silica tube was placed in a furnace that had been preheated to 700 °C and was allowed to soak for 20 min in order to fully melt the excess antimony flux. The fused-silica tube was then removed from the furnace and centrifuged. Following centrifugation, there were black columnar crystals of $OsSb_2$, as well as silver polyhedral crystals of antimony and polycrystalline antimony. The yield of $OsSb_2$ was 100% based on osmium according to powder X-ray diffraction. Residual antimony can be removed from the sample by dissolution in a 1:1:1 mixture of HCl, HNO_3, and H_2O, followed by gravity filtration and rinsing with H_2O and acetone to isolate the crystals of $OsSb_2$.

Scanning Electron Microscopy (SEM). The microprobe analyses of several crystals of each compound were performed with a Hitachi S-4700-II scanning electron microscope using an EDAX Phoenix X-ray energy-dispersive spectrometer. The spectrometer utilizes a lithium-drifted silicon detector with an ultrathin window, and data were acquired with a beam current of 10 μA at 20 kV accelerating potential. Semiquantitative analysis by energy-dispersive spectrometry (EDS) on several crystals of each composition using the Os Mα, P Kα, As Lα, and Sb Lα lines confirmed the 1:2 ratio of osmium and pnicogen elements.

Single-Crystal X-ray Diffraction. Single crystals were selected and mounted on the tips of glass fibers for X-ray diffraction. For OsP_2, intensity data were collected at 120 K using ω scans on a STOE IPDS-II imaging plate diffraction system using graphite-monochromatized Mo Kα radiation (λ = 0.71073 Å) operating at 50 kV and 40 mA with a 34-cm-diameter imaging plate. Individual frames were collected with a 6 min exposure time and a 0.5° ω rotation. For $OsAs_2$ and $OsSb_2$, intensity data were collected at 298 K using ω scans on a STOE 2T imaging-plate diffraction system using graphite-monochromatized Mo Kα radiation (λ = 0.71073 Å) operating at 50 kV and 40 mA with a 34-cm-diameter imaging plate. Individual frames were collected with either a 7 min ($OsAs_2$) or a 4 min ($OsSb_2$) exposure time and either a 1.0° ($OsAs_2$) or a 0.3° ($OsSb_2$) ω rotation. *X-AREA*, *X-RED*, and *X-SHAPE* software packages were used for data collection, integration, and analytical absorption corrections, respectively.[17] Structures were solved with the direct methods program *SHELXS* and refined with the full-matrix least-squares program *SHELXL*.[18] Each final refinement included a secondary extinction correction.

The lattice constants for the $OsPn_2$ compounds determined in the present study (Table 1) by single-crystal X-ray diffraction agree well with those previously reported from refinements of powder X-ray and neutron diffraction data.[14c,15] The unit cell parameters from Rietveld refinements of powder neutron diffraction data are the following: for OsP_2, a = 5.1012(14) Å, b = 5.9022(13) Å, and c = 2.9183(8) Å; for $OsAs_2$, a = 5.4115(15) Å, b = 6.1900(16) Å, and c = 3.0127(7) Å; for $OsSb_2$, a = 5.9411(10) Å, b = 6.6873(12) Å, and c = 3.2109(7) Å. The only discrepancy is found in the OsP_2 lattice constants, which are slightly smaller in the current study because of the fact that the single-crystal X-ray diffraction data were collected at 120 K, in contrast to the powder neutron diffraction data, which were collected at room temperature.

The parameters for data collection and details of the structure refinements are given in Table 1. Atomic coordinates and thermal displacement parameters (U_{eq}) are given in Table 2, anisotropic thermal displacement parameters are given in Table 3, and selected interatomic distances and angles are given in Table 4.

Table 2. Atomic Coordinates and Equivalent Isotropic Displacement Parameters (Å² × 10³) for $OsPn_2$ (Pn = P, As, Sb)

	Wyckoff	x	y	z	U_{eq}[a]
Os	2a	0	0	0	3(1)
P	4g	0.1614(3)	0.3725(2)	0	3(1)
Os	2a	0	0	0	4(1)
As	4g	0.1702(2)	0.3661(1)	0	5(1)
Os	2a	0	0	0	4(1)
Sb	4g	0.1804(2)	0.3589(1)	0	5(1)

[a] U_{eq} is defined as one-third of the trace of the orthogonalized U_{ij} tensor.

Table 3. Anisotropic Displacement Parameters (Å² × 10³) for $OsPn_2$ (Pn = P, As, Sb)[a]

	U_{11}	U_{22}	U_{33}	U_{12}	U_{13}	U_{23}
Os	3(1)	3(1)	3(1)	0(1)	0	0
P	3(1)	3(1)	4(1)	0(1)	0	0
Os	3(1)	4(1)	6(1)	0(1)	0	0
As	3(1)	4(1)	7(1)	−1(1)	0	0
Os	2(1)	4(1)	4(1)	0(1)	0	0
Sb	3(1)	5(1)	5(1)	−1(1)	0	0

[a] The anisotropic displacement factor exponent takes the form $-2\pi^2[h^2a^{*2}U_{11} + \ldots + 2hka^*b^*U_{12}]$.

Table 4. Selected Interatomic Distances (Å) and Angles (deg) for $OsPn_2$ (Pn = P, As, Sb)

	Pn = P	Pn = As	Pn = Sb
Os−Pn (×2)	2.337(1)	2.4414(9)	2.6312(7)
Os−Pn (×4)	2.374(1)	2.4687(7)	2.6572(6)
Os−Os	2.9041(6)	2.9941(6)	3.2044(6)
Pn−Pn	2.221(3)	2.478(2)	2.857(1)
Pn−Os	2.337(1)	2.4414(9)	2.6312(7)
Pn−Os (×2)	2.374(1)	2.4687(7)	2.6572(6)
Pn···Pn	2.9041(6)	2.9941(6)	3.2044(6)
Pn−Os−Pn	75.44(4)	74.66(3)	74.17(2)
Pn−Os−Pn	87.67(3)	87.84(2)	88.05(1)
Pn−Os−Pn	180.0	180.0	180.0
Os−Pn−Os	75.44(4)	74.66(3)	74.17(2)
Pn−Pn−Os	108.86(7)	108.27(4)	107.37(4)
Pn−Pn−Os	111.83(9)	109.67(5)	107.48(3)
Os−Pn−Os	123.37(4)	125.64(2)	128.00(2)

Powder X-ray Diffraction. The phase purity of the products was confirmed by powder X-ray diffraction. The samples were finely ground and mounted on a flat-plate sample holder. Data were collected on a Panalytical X'pert Pro diffractometer with an iron-filtered Cu Kα source, operating at 45 kV and 40 mA under a continuous scanning method in the angular range 2θ = 15−85° in steps of 0.0167°.

Raman Spectroscopy. Raman spectroscopy was performed using a Renishaw inVia Raman microscope with a CCD detector. A polycrystalline sample of OsP_2 (from tin flux) was irradiated by a 532 nm laser at room temperature, and data were collected as an average of five scans.

IR and UV−vis−NIR Diffuse-Reflectance Spectroscopy. The IR spectrum of polycrystalline $OsSb_2$ was measured by using a Thermo Scientific Nicolet 6700 Fourier transform infrared spectrometer in the

dx.doi.org/10.1021/ic501733z | Inorg. Chem. 2014, 53, 9959−9968

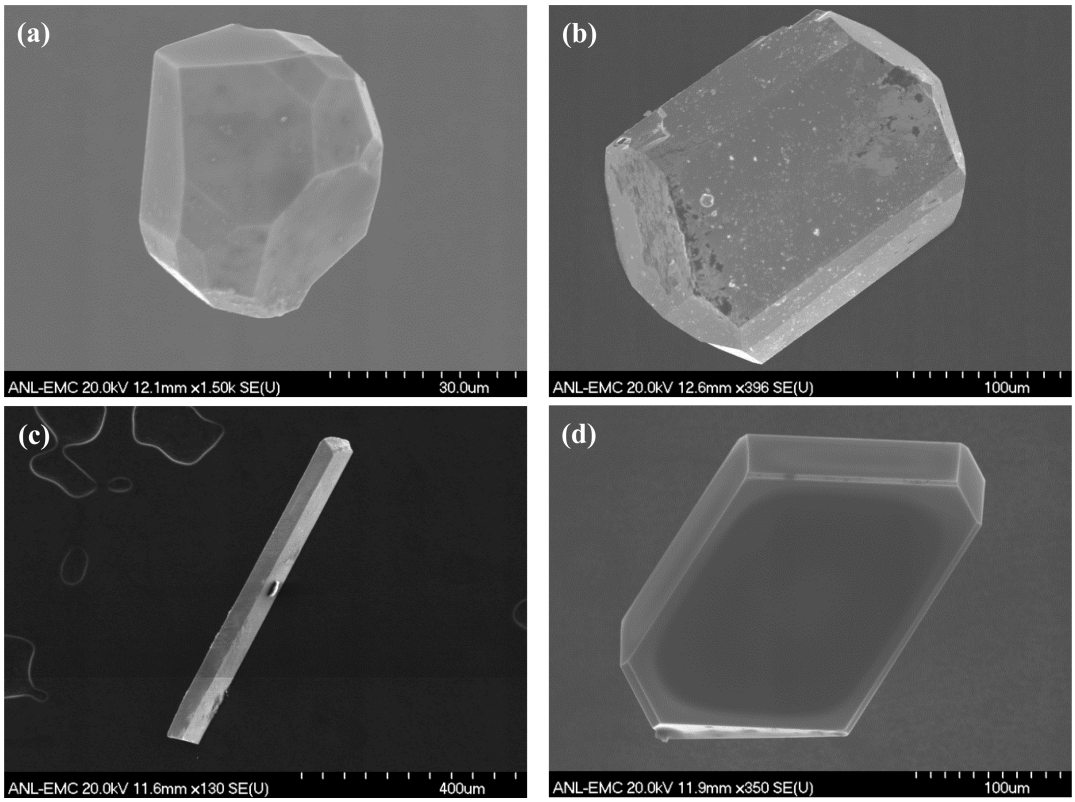

Figure 1. SEM micrographs of typical crystals of (a) OsP_2, (b) $OsAs_2$, (c) $OsSb_2$, and (d) antimony.

range 400−4000 cm^{-1} at room temperature. The UV−vis−NIR spectra of polycrystalline OsP_2 and $OsAs_2$ (both from synthesis with I_2 mineralizer) were recorded with a Shimadzu UV3600 spectrometer in the range 200−2500 nm at room temperature. Reflectance versus wavelength data were used to estimate the band gaps of the materials by converting reflectance to absorption data according to the Kubelka−Munk equation, $\alpha/S = (1 - R)^2/2R$, where R is the reflectance and α and S are the absorption and scattering coefficients, respectively.[19]

Charge-Transport Measurements. Two-probe high-temperature electrical resistivity measurements were performed under vacuum from 300 to 700 K. The two-probe geometry was accomplished with 14 μm (OsP_2 and $OsAs_2$) or 50 μm ($OsSb_2$) gold wires attached to the single crystals via silver paste (DuPont 4929N). A homemade resistivity apparatus equipped with a nanovoltmeter (Keithley 2182A), an electrometer (Keithley 6514), and a high-temperature vacuum chamber governed by a temperature controller (MMR Technologies K-20) was utilized. Thermopower measurements were performed using a commercial MMR Technologies SB-100 Seebeck measurement system under vacuum from 300 to 500 K. A single crystal of $OsSb_2$ was used for the measurement, but no crystals of OsP_2 or $OsAs_2$ with sufficient size were available. Therefore, pure polycrystalline samples of OsP_2 and $OsAs_2$ obtained from tin flux were pressed into pellets and annealed at 1050 °C for 24 h to obtain dense samples for the measurement. The samples were mounted on the stage and attached to the thermocouples with colloidal silver liquid (Ted Pella, Inc., 16031). The Seebeck voltage $V(T)$ was measured by the integral method, in which one end of the sample is held at fixed temperature T_0 and the other end is varied through the temperature T range of interest. The Seebeck coefficient S was obtained from the slope of the $V(T)$ versus T curve, i.e., $S = dV(T)/dT$.[20]

Band Structure Calculations. The band structures of $OsPn_2$ (Pn = P, As, Sb) were studied using density functional theory (DFT) calculations, as implemented in the Vienna Ab initio Simulation Package.[21] We used the projector-augmented-wave method[22] and the Perdew−Burke−Ernzerhof[23] and Heyd−Scuseria−Ernzerhof (HSE06)[24] exchange-correlation functionals. The plane-wave energy cutoff and total energy accuracy were set at 400 and 10^{-3} eV, respectively. The Brillouin zone was sampled with Monkhorst−Pack schemes having a k-mesh of 10 × 10 × 20 for self-consistent calculations and 20 × 20 × 40 to obtain the densities of states. Preliminary studies indicate that spin−orbit interactions have very small effects on the electronic structure and have therefore been neglected in this work.

RESULTS AND DISCUSSION

Synthesis. Metallic fluxes have historically been applied with great success in the crystal growth of pnictide compounds.[25] Because of the volatility of the lighter pnicogens, phosphorus and arsenic, it is difficult to grow single crystals of materials containing these elements without a low-melting metallic flux to properly dissolve the elemental reagents and encourage crystal growth. Phosphides and arsenides have been grown primarily with the use of excess tin or lead; crystals of antimonides have been isolated from reactions with antimony (self-flux) or tin. The main issue to be aware of when using tin flux to grow antimonide single crystals is that tin is oftentimes incorporated into the final product, where it can easily substitute on the antimony atomic sites because of their similar atomic radii.[26]

Single crystals of OsP_2 were initially obtained in low yield from a tin flux reaction with strontium, osmium, and phosphorus with the intent of producing a ternary phase. A rational synthesis omitting strontium was then developed, whereby a 1:2.5 ratio of osmium to phosphorus was reacted in a large excess of tin flux at 1050 °C for 24 h, followed by slow cooling to room temperature. The tin flux could then be removed by briefly heating at 520 °C to liquefy the tin, followed by centrifugation. The product consisted of OsP_2 in the form of both small black prismatic crystals (Figure 1a) and

dx.doi.org/10.1021/ic501733z | Inorg. Chem. 2014, 53, 9959−9968

black polycrystalline material. A similar reaction procedure instead using a 1:12 ratio of osmium to phosphorus, again with a tin flux, was also attempted. The purpose of this reaction was to grow single crystals of the previously reported phases α-OsP_4 or β-OsP_4, whose structures had only been determined via indexing of powder X-ray diffraction data.[27] Some silver platelike crystals were obtained, but the majority of the product was black polycrystalline material. According to powder X-ray diffraction, this sample contained Sn_4P_3, OsP_2, and residual tin. Substituting arsenic in place of phosphorus and reacting with osmium in an excess of tin using a comparable heating profile yielded black prismatic crystals of $OsAs_2$ (Figure 1b).

An initial attempt to grow crystals of $OsSb_2$ with tin flux via the same protocol as that used for OsP_2 and $OsAs_2$ instead resulted in the formation of Os_3Sn_7 as the major phase. To avoid this phase, excess antimony was utilized as a self-flux. Heating osmium with a large excess of antimony in a niobium tube did produce $OsSb_2$, albeit as a polycrystalline material, along with black columnar crystals of $NbSb_2$. It appears that the antimony flux readily reacts with the niobium tube to instead form crystals of $NbSb_2$ (incidentally, the first report of the growth of $NbSb_2$ single crystals was from the reaction of potassium, manganese, and antimony in a niobium tube).[28] By instead performing the reaction of osmium with antimony flux directly in a quartz tube, no impurities (tin and niobium) were present, and large black rodlike crystals (Figure 1c) of $OsSb_2$, which were easily distinguishable from the silvery prisms of antimony (Figure 1d), could be obtained in high yield.

Crystal Structure. The $OsPn_2$ (Pn = P, As, Sb) compounds crystallize in space group *Pnnm* of the orthorhombic crystal system, with the marcasite-type structure. The marcasite crystal structure is closely related to those of rutile and CdI_2. Beginning with a hexagonal close-packed array of anions, half of the octahedral sites should be filled with cations. In the CdI_2 structure type, completely filled cationic layers alternate with completely empty "cationic" layers, so that 50% of the total octahedral sites are filled by cations. In the rutile and marcasite structure types, the octahedral sites in each of the cationic layers are 50% filled. The coordination octahedra surrounding the cations are slightly tilted in rutile and marcasite but in opposite directions such that there is bonding between anions in marcasite but no bonding between anions in rutile.

The crystal structure of the $OsPn_2$ compounds (Figure 2) is a three-dimensional framework of severely distorted $OsPn_6$ octahedra, each of which features two short axial and four long equatorial Os−Pn bonds (Table 4). Within the framework, each octahedron shares two edges (in the *c* direction) and six corners with neighboring octahedra. Each pnicogen atom is four-coordinate, making one bond to a neighboring pnicogen atom and three bonds to osmium atoms, in order to complete a distorted tetrahedral geometry.

The marcasite-type crystal structure can be further subdivided into two classes (Table 5).[3b] First, there are the "regular" marcasites, where the cation has an electronic configuration d^n such that $n \leq 4$, and the *c*/*a* ratio for the unit cell parameters is within the range 0.53−0.57. Conversely, there are the "anomalous" marcasites, which contain a d^n cation where $n \geq 6$, and the *c*/*a* ratio is between 0.73 and 0.75. The difference between the regular and anomalous marcasites is due to the occupation (or lack thereof) of the d_{xy} orbitals in the octahedral environment of the transition-metal cation. In the regular marcasites, the d_{xy} orbital, which points along the *c* axis, is empty, so there is less repulsion between neighboring d transition-metal cations and the M−Pn−M angle is less than 90°. For the anomalous marcasites, a pair of electrons fills the d_{xy} orbital, increasing the repulsion between the transition-metal cations and the M−Pn−M angle is greater than 90°.

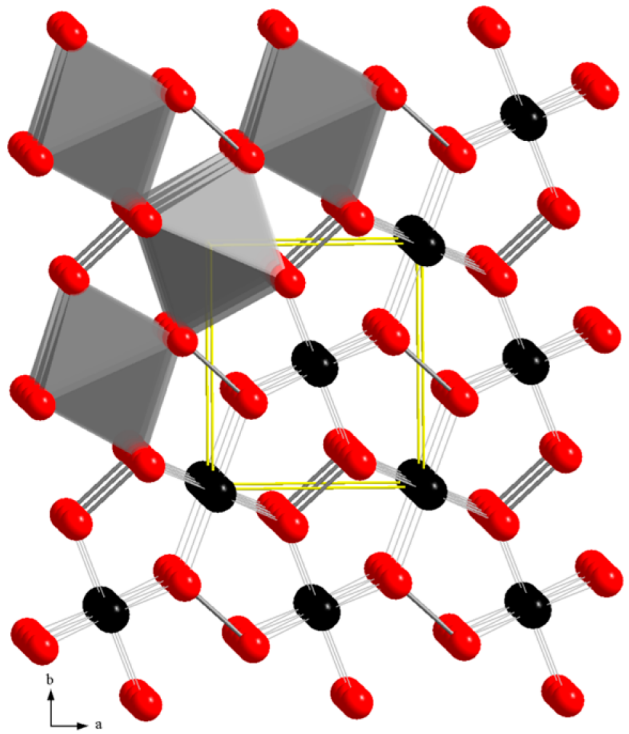

Figure 2. Crystal structure of the marcasite-type $OsPn_2$ (Pn = P, As, Sb) compounds as viewed along the *c* axis. Osmium atoms are represented by black spheres and dark-gray octahedra, and pnicogen atoms are shown as red spheres. Os−Pn bonds are represented by thin gray lines, and Pn−Pn bonds are shown as thick gray lines.

Table 5. Representative Listing of "Regular" and "Anomalous" Marcasites

compound	electronic configuration	*c*/*a*	M−Pn−M angle (deg)	type of marcasite	ref
$CrSb_2$	d^2	0.543	74.66(6)	regular	28
FeP_2	d^4	0.548	72.9(7)	regular	14c
$FeAs_2$	d^4	0.544	74.3(1)	regular	29
$FeSb_2$	d^4	0.548	75.97(4)	regular	30
RuP_2	d^4	0.561	74.53(7)	regular	31
$RuAs_2$	d^4	0.547	73.94(10)	regular	31
$RuSb_2$	d^4	0.534	73.78(7)	regular	31
OsP_2	d^4	0.571	75.44(4)	regular	this work
$OsAs_2$	d^4	0.554	74.66(3)	regular	this work
$OsSb_2$	d^4	0.540	74.17(2)	regular	this work
FeS_2	d^6	0.762	97.5(2)	anomalous	32
$FeSe_2$	d^6	0.747	97.53(7)	anomalous	29
$FeTe_2$	d^6	0.736	97.7(2)	anomalous	32
$RuTe_2$	d^6	0.759	99.031(9)	anomalous	33
β-$NiAs_2$	d^6	0.745	95.5(1)	anomalous	29
$NiSb_2$	d^6	0.741	96.7(1)	anomalous	29
$CoSe_2$	d^7	0.744	97.147	anomalous	34
$CoTe_2$	d^7	0.733	97.2(3)	anomalous	32
CuS_2	d^9	0.759	96.94(1)	anomalous	35
$CuSe_2$	d^9	0.750	94.15(6)	anomalous	29

dx.doi.org/10.1021/ic501733z | Inorg. Chem. 2014, 53, 9959−9968

According to the observed c/a ratios and the M−Pn−M angles, the current $OsPn_2$ compounds should be properly characterized as regular marcasites. Each pnicogen atom in the current compounds forms a single bond to a neighboring pnicogen atom, so they can be formally viewed as $[Pn_2^{4-}]$ anions. In order to achieve charge electroneutrality, the osmium atom would have to have a +4 oxidation state, which results in a d^4 electronic configuration. The d^4 electronic configuration is self-consistent with the classification of these materials as regular marcasites.

Raman Spectroscopy. According to group theory, there are six Raman-active modes for the marcasite-type crystal structure in space group *Pnnm* of the orthorhombic crystal system.[36] Of these six modes, two are X−X stretching vibrations [$A_g(\nu)$ and $B_{1g}(\nu)$], while the other four are X_2 librations [$A_g(R)$, $B_{1g}(R)$, $B_{2g}(R)$, and $B_{3g}(R)$], where X is the chalcogen or pnicogen. For example, the Raman bands observed in the spectrum of FeP_2 at 482, 459, 435, 404, 403, and 403 cm^{-1} have been assigned as $B_{1g}(\nu)$, $B_{1g}(R)$, $A_g(\nu)$, $B_{3g}(R)$, $A_g(R)$, and $B_{2g}(R)$ modes, respectively. However, the bands at 404 and 403 cm^{-1} overlap, so there may only appear to be four total bands in the spectrum.

The Raman spectrum obtained from a polycrystalline sample of OsP_2 at room temperature is shown in Figure 3. There are

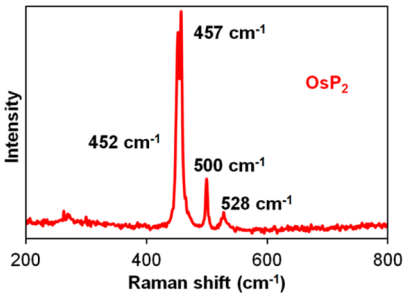

Figure 3. Raman spectrum of OsP_2 at room temperature.

visible Raman bands at 452, 457, 500, and 528 cm^{-1} (with a small shoulder at ~527 cm^{-1}). This is consistent with the reported Raman spectrum for FeP_2, although the values have shifted to higher wavenumbers in OsP_2, which is to be expected for the heavier osmium. Moreover, these values are within the range (350−580 cm^{-1}) typically found for P−P single bonds[37] and less than the values observed for double bonds (~610 cm^{-1}) or triple bonds (~775 cm^{-1}).[38] Along with the P−P bond distance of 2.9041(6) Å from the single-crystal X-ray structure refinement, this confirms that the P−P bond in marcasite-type OsP_2 is indeed a single bond, which further validates the formal assignment of oxidation states in the compound as $[P_2^{4-}]$ and Os^{4+}.

IR and UV−vis−NIR Diffuse-Reflectance Spectroscopy. The binary marcasite-type osmium pnictides are expected to be valence precise compounds with charge-balanced formulas $(Os^{4+})(Pn_2^{4-})$. Bond-length arguments from the single-crystal X-ray structure determination and the Raman spectrum for OsP_2 support the formation of single bonds between the pnicogen atoms to form a dipnictide anion with a formal charge of −4. In order to achieve charge balance, osmium must have a formal oxidation state of +4, which is consistent with the diamagnetism exhibited by these materials.

As valence-precise compounds, these phases are expected to be semiconductors, and, in fact, optical band gaps are observed for all three compounds. From IR diffuse-reflectance spectroscopy, the band gap of $OsSb_2$ is determined to be 0.21(1) eV at room temperature (Figure 4a). The band gaps of $OsAs_2$ and

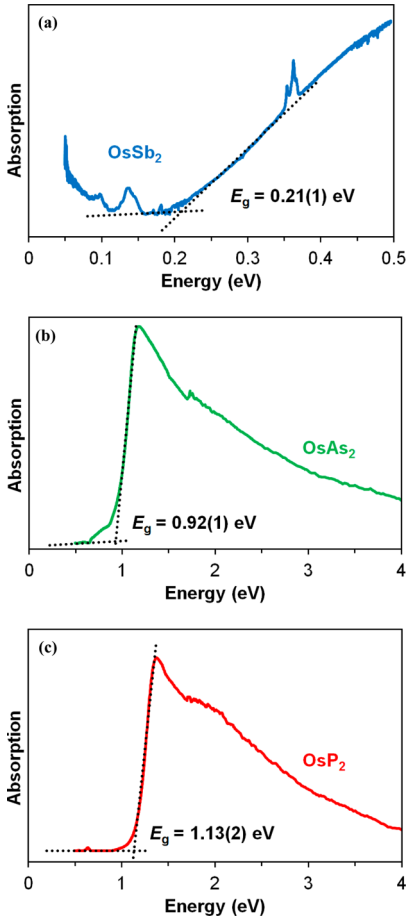

Figure 4. IR spectrum of $OsSb_2$ (a) and UV−vis−NIR spectra for $OsAs_2$ (b) and OsP_2 (c), measured at room temperature, showing the experimentally determined optical band gaps.

OsP_2 are assigned values of 0.92(1) and 1.13(2) eV, respectively, as shown in the UV−vis−NIR diffuse-reflectance spectra (Figure 4b,c). The decreasing band-gap trend in going from the phosphorus to antimony analogue is reasonable and consistent with the band broadening occurring as the pnicogen size increases. The presence of a band gap in these materials, and the trend in size is also predicted by the electronic structure calculations, and the semiconductor behavior is observed in the electrical resistivity data (see below).

Charge-Transport Properties. The electrical resistivity, as measured on single crystals of OsP_2, $OsAs_2$, and $OsSb_2$ in the temperature range 300−700 K, is shown in Figure 5. As expected from previous room temperature measurements on sintered powder samples,[16a] as well as our own electronic band structure calculations (see below), all three compounds are semiconductors. The room temperature electrical resistivity values are 6.408(3), 0.6(2), and 0.90(1) Ω cm for OsP_2, $OsAs_2$, and $OsSb_2$, respectively. These values compare well with those reported for other marcasite-type pnictides, including 0.26 Ω cm for RuP_2 and 0.23−0.63 Ω cm for $RuSb_2$.[39]

The electrical resistivity of OsP_2 decreases from 300 to 400 K, before nearly leveling out in the range 400−550 K, followed by once again decreasing from 550 to 700 K. These three

dx.doi.org/10.1021/ic501733z | Inorg. Chem. 2014, 53, 9959−9968

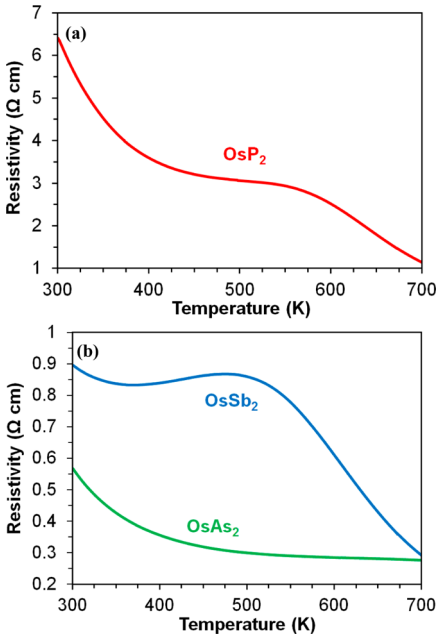

Figure 5. Electrical resistivity as a function of the temperature as measured on single crystals of (a) OsP_2 and (b) $OsAs_2$ and $OsSb_2$.

temperature regimes would seem to correspond to the change in the semiconducting behavior from extrinsic to exhaustion to intrinsic. The thermal activation energy for a semiconductor can be obtained from the Arrhenius equation $\rho = \rho_0 \exp(E_a/k_BT)$, where ρ is the resistivity, E_a is the thermal activation energy, k_B is the Boltzmann constant, and T is the temperature. Linear fits to the data (ln ρ vs $1/T$) for OsP_2 (Figure 6a) yield thermal activation energies E_a = 0.062(1) and 0.327(3) eV over the temperature ranges 300−400 and 625−700 K, respectively. It should be noted that, even at the highest temperature of the measurement, the resistivity of OsP_2 is still decreasing.

$OsAs_2$ exhibits ideal semiconductor behavior where the resistivity decreases over the entire temperature range under investigation. The calculated thermal activation energies are E_a = 0.045(2) and 0.010(3) eV within the temperature ranges 300−450 and 540−700 K, respectively (Figure 6b). The extremely low value of the thermal activation energy for $OsAs_2$, compared with the optical band gap, may indicate that it remains in the exhaustion regime and has not yet achieved intrinsic behavior. The electrical resistivity of $OsSb_2$ is similar to that of OsP_2, in that it displays clear transitions from the extrinsic to exhaustion to intrinsic semiconducting regimes. Initially, the resistivity decreases from 300 to 370 K, followed by a very slight increase (almost negligible) with temperature up to 475 K, before again decreasing through the maximum temperature of 700 K. Linear Arrhenius fits to the data (Figure 6c) result in thermal activation energies E_a = 0.012(7) and 0.272(3) eV over the temperature ranges 300−350 and 600−700 K, respectively. Although the electrical resistivity of $OsSb_2$ is higher than that of $OsAs_2$ at room temperature, their resistivities are nearly equal at the highest temperature (700 K) of the measurement. Furthermore, whereas the resistivity of $OsAs_2$ has nearly leveled off at 700 K, the resistivity of $OsSb_2$ still appears to be decreasing rather substantially at that temperature.

The Seebeck coefficient, as determined for pressed pellets of OsP_2 and $OsAs_2$ and a single crystal of $OsSb_2$, is shown in Figure 7 as a function of the temperature in the range 300−500

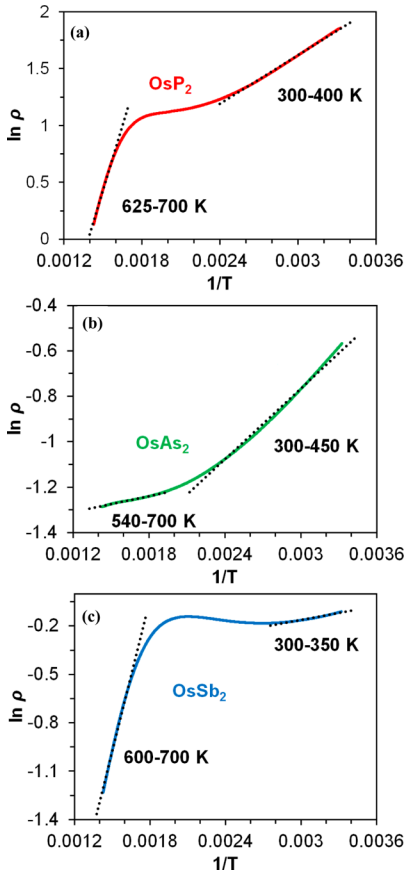

Figure 6. Plots of ln ρ versus $1/T$ and the least-squares fit to the data for (a) OsP_2, (b) $OsAs_2$, and (c) $OsSb_2$.

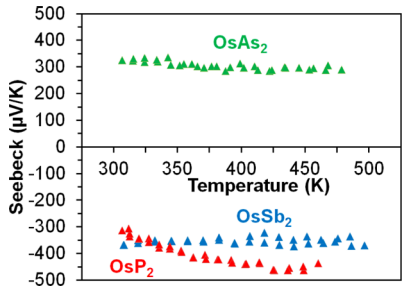

Figure 7. Variable-temperature thermopower data for OsP_2, $OsAs_2$, and $OsSb_2$.

K. The room temperature Seebeck coefficients are approximately −315, 325, and −365 μV K^{-1} for OsP_2, $OsAs_2$, and $OsSb_2$, respectively. Whereas the Seebeck coefficient remains approximately constant for $OsAs_2$ and $OsSb_2$ over the entire temperature range, the Seebeck coefficient of OsP_2 decreases to a value of ∼−460 μV K^{-1} at a temperature of 450 K. From the sign of the Seebeck coefficients, it can be concluded that the dominant charge carriers are electrons (n-type) for OsP_2 and $OsSb_2$, whereas $OsAs_2$ has holes (p-type) as charge carriers. For comparison, the room temperature Seebeck coefficients for some other marcasite-type pnictides include −250 μV K^{-1} for $FeAs_2$,[12] 40 μV K^{-1} for $FeSb_2$,[4a] −170 μV K^{-1} for RuP_2,[39a] and −274 μV K^{-1} for $RuSb_2$.[39b]

Band Structure. The electronic band structures of $OsPn_2$ compounds calculated within the generalized gradient approximation (GGA) are given in Figure 8. All three compounds are

dx.doi.org/10.1021/ic501733z | Inorg. Chem. 2014, 53, 9959−9968

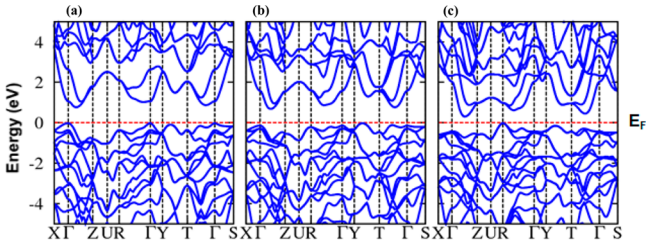

Figure 8. Electronic band structures of (a) OsP_2, (b) $OsAs_2$, and (c) $OsSb_2$, calculated using GGA.

indirect band-gap semiconductors with the valence band maxima at the Γ point for OsP_2, along the YT direction for $OsAs_2$, and at the R point for $OsSb_2$. The conduction band minima (CBM) are along the ΓZ direction for all three compounds. The valence bands (and higher conduction bands) form out of strong hybridization of Os d and Pn p orbitals, whereas the lowest conduction band (LCB) is basically a weakly bonded Os d orbital. This is why the CBM is very similar for all three compounds. The indirect band gaps in GGA (for the relaxed structure) are 0.78, 0.71, and 0.33 eV for OsP_2, $OsAs_2$, and $OsSb_2$, respectively. The corresponding direct band gaps are 1.03, 0.90, and 0.75 eV. Interestingly, the GGA values of the direct band gaps agree very well with experiment for the phosphide and arsenide, whereas the agreement for the antimonide is quite poor. Further theoretical work is necessary to understand the difference between experiment and GGA calculations. When a partial nonlocal exchange (HSE06 functional) is used, the corresponding indirect band gaps increase to 1.52, 1.30, and 0.74 eV. Nonlocal exchange increases the indirect band gap by approximately 0.6−0.7 eV, while the direct band gaps are larger by ∼0.2−0.4 eV. Experimental band gaps associated with charge transport have been estimated from the resistivity measurements in the ranges 300−400 and 600−700 K. The gaps estimated from the resistivity measurements ($E_g \sim 2E_a$) near room temperature are 0.124, 0.09, and 0.024 eV for OsP_2, $OsAs_2$, and $OsSb_2$, respectively, which display the correct trend but are much smaller than the theoretical values (especially those calculated with HSE06, which are reported to give good values of band gaps for many known semiconductors[24]). Band gaps estimated from the resistivity measurements at higher temperatures (600−700 K) are 0.654, 0.02, and 0.544 eV for the three compounds. The result for $OsAs_2$ is anomalous, but the gap values for the other two compounds are consistent with the GGA results. A comparison between the theoretical and experimental transport band-gap values clearly shows the dominance of defects. This large discrepancy may imply that the energy gaps estimated from the resistivity measurements at lower temperatures are most likely from extrinsic defects.

The total and projected DOS for the $OsPn_2$ compounds are shown in Figure 9. These DOSs are very similar to those of the isostructural marcasites $FePn_2$ and $RuPn_2$. In these systems, the valence orbitals/occupancies are d^6s^2 for the metal (M) atoms and s^2p^3 for the Pn atoms. The orthorhombic unit cell is highly compressed along the *c* axis, resulting in a *c*/*a* ratio of less than 0.6 and an M−Pn−M angle considerably less than 90° (Table 5). The distortion of the MPn_6 octahedra and the *c*-axis compression are intimately related to and controlled by the d occupation (nearly d^4). There is strong hybridization between the M d and Pn p orbitals. Considering the total manifold of valence states, there are 5 + 2 × (3 + 1) = 13 states/formula

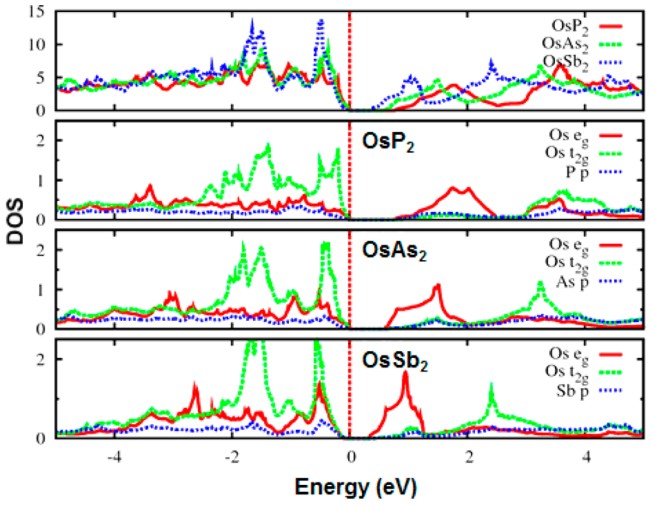

Figure 9. Total and projected DOSs for OsP_2, $OsAs_2$, and $OsSb_2$.

unit. The total number of valence electrons is 18 valence electrons/formula unit, which occupy only 9 of the 13 total bands, indicating that these are, in fact, semiconductors. However, it is not clear whether the 18-electron rule is operative in the formation of band gaps in these systems as in the half-Heusler compounds such as ZrNiSn or ZrCoSb.[40]

Choosing the energy of the highest occupied state as the zero of energy, some general characteristics can be gleaned from an examination of the DOSs over a broad energy range. Pn s bands lie at ∼−10 eV (not shown here) with a width of ∼5 eV, which is rather large and indicates substantial hybridization and overlap (Pn−Pn bonding). The Os d and Pn p bands span an energy range from −6.0 to +7.5 eV. Ignoring the narrow energy band (width ∼1.0 eV) centered about 0.5 eV, which constitutes the LCB, there is a hybridization gap around 1−1.5 eV for $OsSb_2$. The LCB (bottom 2 eV) is a weakly bonding Os d orbital, which essentially has a quasi-one-dimensional character with stronger dispersion along the *c* axis. This part of the DOS is common to all three compounds. As seen in Figure 9, the bandwidth of Os e_g bands decreases on moving from phosphorus to arsenic to antimony, implying smaller overlap between Os e_g orbitals. This is consistent with an increase in the lattice parameters from OsP_2 to $OsAs_2$ to $OsSb_2$. Although the upper part of the valence band (highest valence band, HVB) is also similar for all three compounds, the position of the maxima differ from one to the others because of subtle differences in d−p hybridization effects. These characteristics of the LCB and HVB are reflected in their thermoelectric properties, as discussed next.

The thermopowers (Seebeck coefficients, *S*) calculated from GGA electronic band structures are plotted as a function of the temperature in Figure 10. The $OsPn_2$ phases are predicted to have large Seebeck coefficient values (larger than that of the state-of-the-art thermoelectric material PbTe) because of multiple carrier pockets in the first Brillouin zone. The *S* curves have turnovers at ∼500 K due to bipolar effects. The turnover points shift to lower temperatures on moving from phosphorus to arsenic to antimony because of a decrease in the band gap. It is noteworthy that GGA usually underestimates the band gaps (as mentioned above, HSE06 provides larger band gaps); thus, the experimental turnover points should be expected to occur at even higher temperatures. While the *S* curves are quite symmetrical for $OsSb_2$ (n- and p-type *S* curves

dx.doi.org/10.1021/ic501733z | Inorg. Chem. 2014, 53, 9959−9968

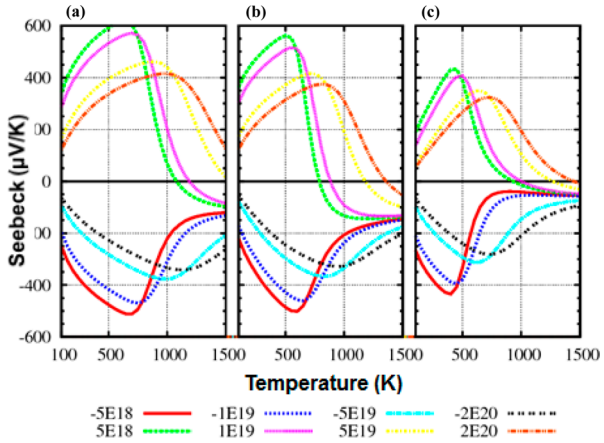

Figure 10. Thermopower as a function of the temperature at different carrier concentrations for (a) OsP_2, (b) $OsAs_2$, and (c) $OsSb_2$, calculated using Boltzmann's transport equation. The carrier concentrations (bottom) are given in units of cm^{-3}.

are similar), the S curves are larger for p-type OsP_2 and $OsAs_2$. This difference can be understood by examining the band structures in Figure 8. While $OsSb_2$ has only 2-fold degenerate hole pockets at R and along the YT direction, OsP_2 and $OsAs_2$ have additional hole pockets at Γ points and along the ΓT directions, thereby increasing the degeneracy and hence yielding larger Seebeck coefficient values for the same carrier concentration. The large theoretical values of the magnitude of S at room temperature for accessible carrier concentration ranges are consistent with our experimental values. The fact that at room temperature OsP_2 and $OsSb_2$ are n-type, whereas $OsAs_2$ is p-type, has to do with extrinsic defects as observed in the resistivity measurements.

CONCLUSION

The binary osmium pnictides, $OsPn_2$, can be grown from tin flux for the phosphorus and arsenic analogues, and antimony self-flux for the antimony compound. These materials crystallize in the well-known marcasite-type structure, with a three-dimensional framework of corner- and edge-sharing $OsPn_6$ octahedra, interconnected by Pn−Pn dimers. Raman spectroscopy and electronic structure calculations confirm that there is a single bond between the phosphorus atoms in the dipnictide anions of OsP_2. Optical absorption spectroscopy (IR and UV−vis−NIR) and electrical resistivity data identify these materials as narrow-band-gap semiconductors with band gaps of 1.13(2), 0.92(1), and 0.21(1) eV for OsP_2, $OsAs_2$, and $OsSb_2$, respectively. Nominally undoped OsP_2 and $OsSb_2$ are n-type semiconductors, but $OsAs_2$ is a p-type semiconductor, as determined from thermopower measurements. Electronic structure calculations confirm that these compounds are narrow-band-gap semiconductors with indirect band gaps. The GGA band gaps agree reasonably well with the values estimated from the resistivity measurements at high temperatures for OsP_2 and $OsSb_2$ but not for $OsAs_2$. This may be related to the p-type transport observed in $OsAs_2$, while the other two exhibit n-type transport. The direct GGA band gaps in OsP_2 and $OsAs_2$ agree very well with those obtained from optical absorption measurements but are approximately a factor of 3.5 larger in $OsSb_2$. To understand these differences, one needs to analyze the type of native defects in these compounds and what roles they play in optical absorption and charge transport. The high thermopower values for these indirect narrow-band-gap semiconductors suggest a possible application as thermoelectric materials. In order to determine the thermoelectric figure of merit (ZT), the thermal conductivities of these compounds must be measured. Furthermore, doping studies to optimize the electrical and thermal transport properties of the $OsPn_2$ phases should be performed if they are indeed to find use as thermoelectric materials.

ASSOCIATED CONTENT

Supporting Information

Crystallographic data in CIF format. This material is available free of charge via the Internet at http://pubs.acs.org.

AUTHOR INFORMATION

Corresponding Author

*E-mail: m-kanatzidis@northwestern.edu. Tel: 847-467-1541. Fax: 847-491-5937.

Notes

The authors declare no competing financial interest.

ACKNOWLEDGMENTS

This work was supported by the U.S. Department of Energy, Office of Science, Materials Sciences and Engineering. Electron microscopy was accomplished at the Electron Microscopy Center at Argonne National Laboratory, a U.S. Department of Energy Office of Science Laboratory operated under Contract DE-AC02-06CH11357 by UChicago Argonne, LLC. Work at Michigan State University was partially supported by the Center for Revolutionary Materials for Solid State Energy Conversion, a DOE EFRC, under Award DE-SC0001054.

REFERENCES

(1) (a) Kamihara, Y.; Watanabe, T.; Hirano, M.; Hosono, H. *J. Am. Chem. Soc.* **2008**, *130*, 3296−3297. (b) Rotter, M.; Tegel, M.; Johrendt, D. *Phys. Rev. Lett.* **2008**, *101*.

(2) Buerger, M. J. *Am. Mineral.* **1931**, *16*, 361−395.

(3) (a) Petrovic, C.; Kim, J. W.; Bud'ko, S. L.; Goldman, A. I.; Canfield, P. C.; Choe, W.; Miller, G. J. *Phys. Rev. B* **2003**, *67*, 155205. (b) Petrovic, C.; Lee, Y.; Vogt, T.; Lazarov, N. D.; Bud'ko, S. L.; Canfield, P. C. *Phys. Rev. B* **2005**, *72*, 045103.

(4) (a) Bentien, A.; Johnsen, S.; Madsen, G. K. H.; Iversen, B. B.; Steglich, F. *Europhys. Lett.* **2007**, *80*, 17008. (b) Jie, Q.; Hu, R.; Bozin, E.; Llobet, A.; Zaliznyak, I.; Petrovic, C.; Li, Q. *Phys. Rev. B* **2012**, *86*, 115121.

(5) (a) Hu, R.; Mitrović, V. F.; Petrovic, C. *Phys. Rev. B* **2006**, *74*, 195130. (b) Hu, R.; Hermann, R. P.; Grandjean, F.; Lee, Y.; Warren, J. B.; Mitrović, V. F.; Petrovic, C. *Phys. Rev. B* **2007**, *76*, 224422.

(6) Hu, R.; Mitrović, V. F.; Petrovic, C. *Phys. Rev. B* **2007**, *76*, 115105.

(7) Sun, P.; Oeschler, N.; Johnsen, S.; Iversen, B. B.; Steglich, F. *Dalton Trans.* **2010**, *39*, 1012−1019.

(8) Bentien, A.; Madsen, G. K. H.; Johnsen, S.; Iversen, B. B. *Phys. Rev. B* **2006**, *74*, 205105.

(9) Hu, R.; Mitrović, V. F.; Petrovic, C. *Phys. Rev. B* **2009**, *79*, 064510.

(10) Kieslich, G.; Birkel, C. S.; Veremchuk, I.; Grin, Y.; Tremel, W. *Dalton Trans.* **2014**, *43*, 558−562.

(11) (a) Silva, D. C. C.; Crosnier, O.; Ouvrard, G.; Greedan, J.; Safa-Sefat, A.; Nazar, L. F. *Electrochem. Solid-State Lett.* **2003**, *6*, A162−A165. (b) Boyanov, S.; Bernardi, J.; Gillot, F.; Dupont, L.; Womes, M.; Tarascon, J.-M.; Monconduit, L.; Doublet, M.-L. *Chem. Mater.* **2006**, *18*, 3531−3538.

(12) Usui, H.; Suzuki, K.; Kuroki, K.; Nakano, S.; Kudo, K.; Nohara, M. *Phys. Rev. B* **2013**, *88*, 075140.

(13) (a) Biltz, W.; Ehrhorn, H.-J.; Meisel, K. *Z. Anorg. Allg. Chem.* **1939**, *240*, 117−128. (b) Wöhler, L.; Ewald, K. F. A. *Z. Anorg. Allg. Chem.* **1931**, *199*, 57−64.
(14) (a) Rundqvist, S. *Nature* **1960**, *185*, 31−32. (b) Holseth, H.; Kjekshus, A. *Acta Chem. Scand.* **1968**, *22*, 3273−3283. (c) Holseth, H.; Kjekshus, A. *Acta Chem. Scand.* **1968**, *22*, 3284−3292.
(15) Kjekshus, A.; Rakke, T.; Andresen, A. F. *Acta Chem. Scand. A* **1977**, *31*, 253−259.
(16) (a) Hulliger, F. *Nature* **1963**, *198*, 1081−1082. (b) Holseth, H.; Kjekshus, A. *J. Less-Common Met.* **1968**, *16*, 472−474.
(17) *X-AREA*, *X-SHAPE*, and *X-RED*; Stoe & Cie GmbH: Darmstadt, Germany, 2009.
(18) Sheldrick, G. H. *Acta Crystallogr., Sect. A: Found. Crystallogr.* **2008**, *64*, 112−122.
(19) (a) Tandon, S. P.; Gupta, J. P. *Phys. Status Solidi B* **1970**, *38*, 363−367. (b) McCarthy, T. J.; Ngeyi, S.-P.; Liao, J.-H.; DeGroot, D. C.; Hogan, T.; Kannewurf, C. R.; Kanatzidis, M. G. *Chem. Mater.* **1993**, *5*, 331−340. (c) Liao, J.-H.; Varotsis, C.; Kanatzidis, M. G. *Inorg. Chem.* **1993**, *32*, 2453−2462.
(20) Wood, C.; Chmielewski, A.; Zoltan, D. *Rev. Sci. Instrum.* **1988**, *59*, 951−954.
(21) (a) Kresse, G.; Furthmuller, J. *Comput. Mater. Sci.* **1996**, *6*, 15−50. (b) Kresse, G.; Furthmuller, J. *Phys. Rev. B* **1996**, *54*, 11169−11186. (c) Kresse, G.; Hafner, J. *Phys. Rev. B* **1993**, *47*, 558−561.
(22) (a) Blöchl, P. E. *Phys. Rev. B* **1994**, *50*, 17953−17979. (b) Kresse, G.; Joubert, D. *Phys. Rev. B* **1999**, *59*, 1758−1775.
(23) Perdew, J. P.; Burke, K.; Ernzerhof, M. *Phys. Rev. Lett.* **1996**, *77*, 3865−3868.
(24) (a) Heyd, J.; Scuseria, G. E.; Ernzerhof, M. *J. Chem. Phys.* **2003**, *118*, 8207−8215. (b) Heyd, J.; Scuseria, G. E. *J. Chem. Phys.* **2004**, *121*, 1187−1192. (c) Heyd, J.; Scuseria, G. E.; Ernzerhof, M. *J. Chem. Phys.* **2006**, *124*, 219906.
(25) (a) Kanatzidis, M. G.; Pöttgen, R.; Jeitschko, W. *Angew. Chem., Int. Ed.* **2005**, *44*, 6996−7023. (b) Canfield, P. C.; Fisk, Z. *Philos. Mag. B* **1992**, *65*, 1117−1123.
(26) (a) Gautreaux, D. P.; Capan, C.; DiTusa, J. F.; Young, D. P.; Chan, J. Y. *J. Solid State Chem.* **2008**, *181*, 1977−1982. (b) Phelan, W. A.; Nguyen, G. V.; DiTusa, J. F.; Chan, J. Y. *J. Alloys Compd.* **2012**, *523*, 176−181.
(27) (a) Braun, D. J.; Jeitschko, W. *Z. Anorg. Allg. Chem.* **1978**, *445*, 157−166. (b) Flörke, U.; Jeitschko, W. *J. Less-Common Met.* **1982**, *86*, 247−253.
(28) Rehr, A.; Kauzlarich, S. M. *Acta Crystallogr., Sect. C: Cryst. Struct. Commun.* **1994**, *50*, 1177−1178.
(29) Holseth, H.; Kjekshus, A.; Andresen, A. F. *Acta Chem. Scand.* **1970**, *24*, 3309−3316.
(30) Kjekshus, A.; Rakke, T.; Andresen, A. F. *Acta Chem. Scand., Ser. A* **1974**, *28*, 996−1000.
(31) Holseth, H.; Kjekshus, A. *Acta Chem. Scand.* **1969**, *23*, 3043−3050.
(32) Brostigen, G.; Kjekshus, A. *Acta Chem. Scand.* **1970**, *24*, 1925−1940.
(33) Köhler, J. *Z. Anorg. Allg. Chem.* **1997**, *632*, 1657−1660.
(34) Ramdohr, P. *Neues Jahrb. Mineral., Monatsh.* **1955**, *6*, 133−143.
(35) Kjekshus, A.; Rakke, T. *Acta Chem. Scand., Ser. A* **1979**, *33*, 617−620.
(36) Lutz, H. D.; Müller, B. *Phys. Chem. Miner.* **1991**, *18*, 265−268.
(37) Nakamoto, K. Inorganic Compounds. In *Infrared and Raman Spectra of Inorganic and Coordination Compounds*, 4th ed.; John Wiley & Sons: New York, 1986.
(38) Schnöckel, H.; Willner, H. Vibrational spectroscopy of different classes and states of compounds: Inorganic substances. In *Infrared and Raman Spectroscopy*; Schrader, B., Ed.; VCH Publishers, Inc.: New York, 1995.
(39) (a) Kaner, R.; Castro, C. A.; Gruska, R. P.; Wold, A. *Mater. Res. Bull.* **1977**, *12*, 1143−1147. (b) Harada, T.; Kanomata, T.; Suzuki, T.; Yoshida, H.; Kaneko, T. *J. Alloys Compd.* **2001**, *317−318*, 287−292. (c) Harada, T.; Kanomata, T.; Takahashi, Y.; Nashima, O.; Yoshida, H.; Kaneko, T. *J. Alloys Compd.* **2004**, *383*, 200−204.
(40) Graf, T.; Felser, C.; Parkin, S. S. P. *Prog. Solid State Chem.* **2011**, *39*, 1−50.